4-Axis 3D-Printed Tubular Biomaterials Imitating the Anisotropic Nanofiber Orientation of Porcine Aortae

Florian Lackner, Paola Šurina, Julia Fink, Petra Kotzbeck, Dagmar Kolb, Jan Stana, Maximilian Grab, Christian Hagl, Nikolaos Tsilimparis, Tamilselvan Mohan, Karin Stana Kleinschek, and Rupert Kargl*

Many of the peculiar properties of the vasculature are related to the arrangement of anisotropic proteinaceous fibers in vessel walls. Understanding and imitating these arrangements can potentially lead to new therapies for cardiovascular diseases. These can be pre-surgical planning, for which patient-specific ex vivo anatomical models for endograft testing are of interest. Alternatively, therapies can be based on tissue engineering, for which degradable in vitro cell growth substrates are used to culture replacement parts. In both cases, materials are desirable that imitate the biophysical properties of vessels, including their tubular shapes and compliance. This work contributes to these demands by offering methods for the manufacturing of anisotropic 3D-printed nanofibrous tubular structures that have similar biophysical properties as porcine aortae, that are biocompatible, and that allow for controlled nutrient diffusion. Tubes of various sizes with axial, radial, or alternating nanofiber orientation along the blood flow direction are manufactured by a customized method. Blood pressure-resistant, compliant, stable, and cell culture-compatible structures are obtained, that can be degraded in vitro on demand. It is suggested that these healthcare materials can contribute to the next generation of cardiovascular therapies of ex vivo pre-surgical planning or in vitro cell culture.

1. Introduction

Biological tissues synthesized, excreted, and maintained by living cells contain protein nanofibrils or filaments. The nanofibrils form highly anisotropic dynamic load-bearing structures. In the human and other mammalian vasculatures, collagen, and elastin fibrils are arranged axially and radially along the axis of blood flow, forming a multi-layered strain-stiffening, elastic, and hydrated mesh.[1] In contrast to most synthetic polymers, biological tissues such as blood vessels, skin, and ligaments become stiffer upon deformation, which is essential to maintain their integrity and physiological functions.[2] Elastin, collagen, fibronectin, proteoglycans, and other components in vascular arteries contribute to these anisotropic networks.[1,3] Upon uniaxial straining, a two-phase response occurs as the interwoven collagen and elastin resist deformation.[4] Vascular tissue is a very soft material at low strain and is highly hydrated, containing ≈70 w% water[3b]

F. Lackner, P. Šurina, T. Mohan, K. Stana Kleinschek, R. Kargl
Institute for Chemistry and Technology of Biobased System (IBioSys)
Graz University of Technology
Stremayrgasse 9, 8010 Graz, Austria
E-mail: rupert.kargl@tugraz.at

J. Fink, P. Kotzbeck
COREMED - Centre of Regenerative and Precision Medicine
JOANNEUM RESEARCH Forschungsgesellschaft mbH
Neue Stiftingtalstraße 2, 8010 Graz, Austria

D. Kolb
Core Unit Ultrastructure Analysis
Medical University Graz
Stiftingtalstraße 6/II, 8010 Graz, Austria

D. Kolb
Gottfried Schatz Research Center for Cell Signaling Metabolism and Aging
Medical University Graz
Stiftingtalstraße 6, 8010 Graz, Austria

J. Stana, N. Tsilimparis
Department of Vascular Surgery
Ludwig Maximilian University Munich
Marchioninistraße 15, 81377 Munich, Germany

M. Grab, C. Hagl
Department of Cardiac Surgery
Ludwig Maximilian University Munich
Marchioninistraße 15, 81377 Munich, Germany

T. Mohan, R. Kargl
Laboratory for Characterization and Processing of Polymers
University of Maribor
Smetanova ulica 16, Maribor 2000, Slovenia

ADVANCED
SCIENCE NEWS

www.advancedsciencenews.com

ADVANCED
HEALTHCARE
MATERIALS

www.advhealthmat.de

which decisively influences its properties. Imitating this arrangement in an artificial tubular form can be of high interest for a basic understanding of such networks, and for ex vivo applications in i) pre-surgical planning or ii) in vitro tissue cultures. For pre-surgical planning, for example, endovascular aneurysm repair (EVAR), patient-specific anatomies obtained from medical imaging could be 3D printed using biomimetic materials that behave like vascular tissue in terms of anisotropic mechanics. These printed specimens could be used to test the implantation and performance of PTFE/PET endografts outside the patient´s body to improve materials and therapy outcomes. Finally, for potential in vitro cell culture, chemical and mechanical properties, fiber anisotropy, and hydration are relevant.[5]

3D (bio-)printing can be a method to fabricate desired shapes comprising said fibrillar networks.[6] Existing 3D printing technology, for example, Stratasys PolyJet produces materials and shapes that are close to heart tissue in punctuation modulus, but very distant from real tissue in terms of strain stiffening, lubricity, water content, compliance and blood flow, sectility, or suturability.[7] A demand therefore exists, to investigate and develop nanofibrillar biomimetic materials. Since the macroscopic stress-strain relation usually observed for tissue in tensile tests differs for many synthetics, finding the right materials, and transferring them into 3D printing is challenging.[8] Most vascular models are made using synthetic polymeric materials such as silicones, thermoplastic elastomers, crosslinked gels, or flexible acrylate urethane resins,[9] which can hardly replicate tissue mechanics and water content.[10] (Semi-)synthetic isotropic (hydro-)gels consisting of flexible polymer chains seldom show sufficient strength and elongation, and they tend to rupture before the polymer chains become straightened, while the entangled chains can easily slip past each other to reduce stress.[11]

An alternative source for biological semirigid filamentous materials that could imitate collagen fibers and add strength and anisotropy is, therefore, nanofibrillar cellulose (NFC), which has bending stiffness and can be chemically modified.[12] NFCs are obtained from bacteria in well-defined shapes,[13] or more heterogeneously from plants.[14] Aqueous entangled NFC suspensions are shear thinning because they do not contain strong covalent cross-links and are highly hydrated. However blends with NFC[15] oxidized NFC[16] or poly(2-hydroxyethyl methacrylate) (pHEMA) grafted NFC[12a,17] have been described, giving a hint that tuning the fibrillar interactions might lead to desired properties of sufficient mechanical strength in a highly hydrated network. Blending with polysaccharides including alginate to crosslink fibrils[18] has been reported also by our group[19], and commercial 3D printing inks are available.[20] Fibrils with a high aspect ratio undergo extensive shear force alignment in extrusion 3D printing. This alignment was used to create objects with anisotropic properties.[21] An extensive body of literature describes the use of NFC/Alginate in 3D printing,[22] including assessments of

their properties in contact with live cells and tissue.[23] Published works, however, focus mainly on flat and easily printable structures. 3D printing of elongated tubular forms remains challenging and such prints do neither have axial or radial nanofiber alignment nor mechanical anisotropy.[24]

To contribute to advances in the field, and to pave the way for manufacturing technology in pre-surgical planning, this work aims to investigate, prepare, and understand anisotropic nanofibrillar networks manufactured into tubes by 4-axis 3D printing (**Figure 1**). The materials should mimic the biomechanical properties of porcine aortic vascular tissue with respect to their fiber orientation, extensibility, and dynamic compliance. Finally, the biocompatibility of the materials is assessed by cell test of leachates and in contact with human cells, whereas permeability of the networks towards compounds with different molar masses and the coagulation of blood plasma proteins in contact with the materials is investigated. A concept is shown on how to disintegrate the otherwise very stable fiber meshes in case the materials are used as possible in vitro tissue culture substrates in future works.

2. Results and Discussion

2.1. Anisotropic Printing Process

It was previously shown that nanofiber orientation in 3D-printed hydrogels can be controlled and determines the anisotropic mechanical response of gels.[19] Transitioning from flat objects to tubular systems while retaining the ability to control the nanofiber orientation is however limited by the printing technology. It is of high interest to replicate the anisotropic mechanical effects observed in the mammalian vasculature in the form of tubular structures.[25] Such tubular structures can be manufactured by extrusion printing on a rotating drum as an auxiliary device (**Figure 2**A). The drum is driven by a stepper motor and controlled electronically. This setup allows for an operation in two different modes which determine the orientation of the nanofibers in the 3D-printed tubes. The first mode is radial printing, in which the drum rotates continuously at a given speed, while the extrusion print head moves in a slow linear motion along the drum´s rotational axis (Figure 2C) (Video S1, Supporting Information). This causes a fiber alignment in the radial direction of the drum due to the extrusion forces and the rotation. The precise interaction between the nozzle diameter, the linear movement of the print head, and the rotational speed of the drum is essential in this process (Supporting Information).

The second mode of operation is axial printing (Figure 2B) (Video S2, Supporting Information), in which the drum rotates only incrementally in accordance with the axial print head movement, nozzle diameter, and strand thickness. Depending on the movement of the print head, axial single or double strands (back and forth) can be printed at each increment. To simplify the coordination between printer movement and drum rotation, a light switch was installed, sending a signal whenever the nozzle passes. Standard printing parameters are a printing speed of 20 to 25 mm s^{-1} at 130 kPa extrusion pressure, with a nozzle diameter of 410 µm, but nozzles with 240 and 580 µm were also successfully tested. By combining the two printing modes, it was also possible to produce tubes with an alternating grid-like

J. Fink, P. Kotzbeck
Research Unit for Tissue Regeneration, Repair and Reconstruction,
Division of Plastic, Aesthetic and Reconstructive Surgery, Department of Surgery
Medical University of Graz
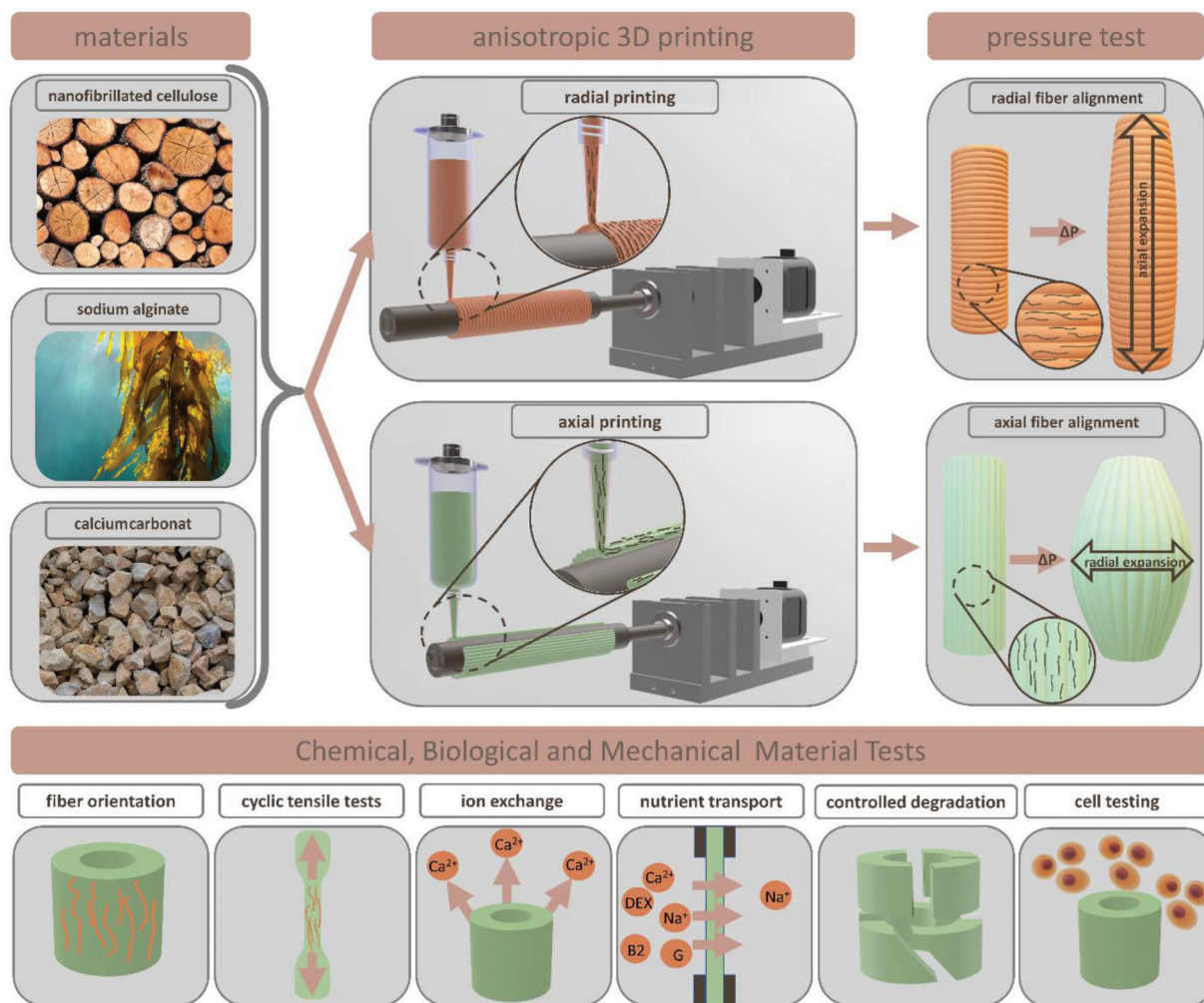Auenbruggerplatz 29/4, 8036 Graz, Austria

Figure 1. Schematic process overview, starting from nano-fibrillated cellulose, alginate, and calcium carbonate mixed to form a homogeneous ink for DIW 3D printing. The radial printing method (orange) results in a tube that expands predominantly in the axial direction due to the radial fiber orientation. This is the opposite of axial printing (green), which results in axial fiber alignment and radial expansion under pressure. After controlling the anisotropy of these tubes, various material characteristics and properties were investigated in detail, such as fiber orientation, cyclic tensile tests, ion exchange, nutrient diffusion, controlled degradation experiments, and cell viability tests which are schematically shown in the lower part of this figure.

axial/radial/axial fiber orientation. Depending on the desired inner tube diameter, different drums ranging from 9 to 22 mm were used. To obtain tubes with a thickness of 2 mm, three superimposed layers were printed with a 410 µm nozzle. It is worth noting that the method of cross-linking after print finalization leads to very stable constructs without any observable delamination of interlayers. With this method, anisotropic tubes with diameters between 9 to 22 mm, and a length of 15 cm can be produced without intermediate crosslinking or additional supports, otherwise common in 3D printing (Figure 2D–F).

2.2. Fiber Orientation and Mechanical Response of the Tubes

2.2.1. Alignment Visualization

During extrusion printing of hydrogels, the shear forces in the nozzle align the fibers towards the direction of the printing path.[21a–d,26] Since the printing path can additionally be controlled by the operating mode of the auxiliary rotary drum, the fiber alignment in the tube wall can be controlled. **Figure 3**A shows the alignment of fluorescence-stained NFCs in dependence on the printing mode and compared to cast samples. For axially printed samples, a clear fiber orientation distribution is visible that fits a Gaussian function with $R^2 \geq 0.98$. A maximum in the fiber orientation angle of $93 \pm 1.1°$ with respect to the drum rotation direction is observed, leading to axially aligned fibers in the tubes. For the radially printed specimen, the fibers are aligned along the drum's rotation direction, whereas casted samples do not show a fiber direction.

2.2.2. Tensile Strength and Moduli

Fiber orientation has a strong influence on the mechanical response of flat objects.[19,21a,c] To compare the tensile strength and
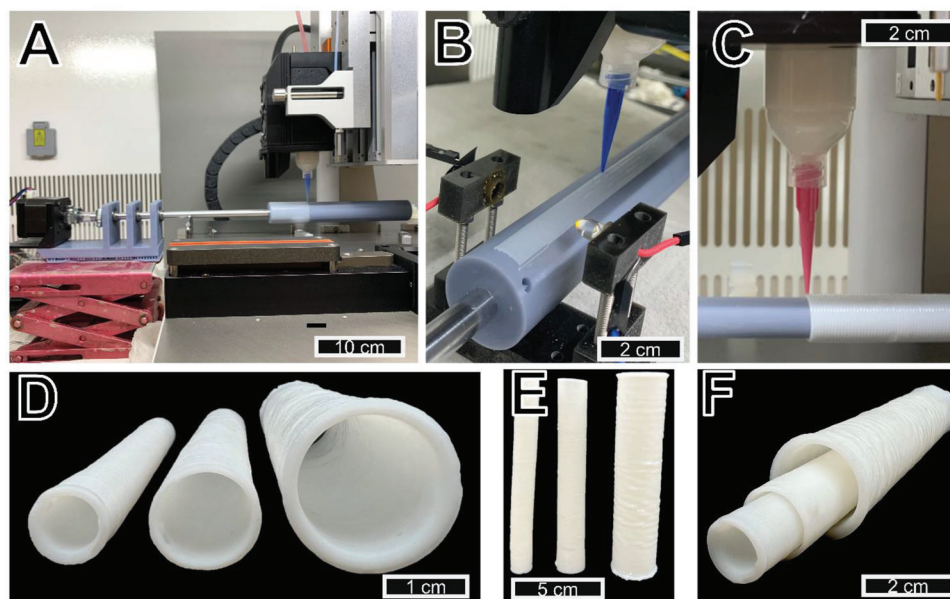
Figure 2. Images of the printing process and printed tubes: A) Image of the radial printing setup consisting of a stepper motor (left), a 3D-printed bearing holder with ball bearings, a linear steel rod, and the rotating drum onto which Ink1.1 is extruded, B) close-up of the axial printing process including the light switch in black, using a blue 410 µm nozzle to extrude the ink, C) close-up of the radial printing method using a pink 580 µm nozzle to extrude the ink, D) printed and crosslinked wet tubes with 9 mm (left), 15 mm (center), and 22 mm (right) inner diameters, E) the same tubes but standing upright, and F) the same tubes stacked in each other.

modulus of porcine aortic tissue with the printed tubes, dog-bone-shaped tensile test specimens were cut from the printed tubes and porcine aortae along the axial and radial directions of the blood flow axis (Figure 3F). The ultimate tensile strength and moduli of the materials reflect the fiber orientation in the tubes, and the cut direction of the tensile test specimen (Figure S2, Supporting Information). The ultimate tensile strength and the strain at break are always higher for the samples measured axially, along the oriented fibers than for those measured perpendicular to it. The fiber alignment obviously enhances the load-bearing capacity, extensibility, and toughness of the network by a parallel displacement of the fibers under tension. A significant difference between the biologically grown porcine tissue and the printed tubes can be seen from the shape of the tensile curves for axially (Figure 3E) or radially printed tubes (Figure 3G) with different cut directions. The printed tubes show a nearly linear stress-strain relation, while the porcine aortae are typically strain-stiffening. With its nonlinear tensile modulus, the porcine aorta appears like a hybrid material between an axially printed tube at low strain and a radially printed tube at high strain. Supposedly this can be attributed to the complex geometry and deformation path of the fiber network in the natural tissue.

The uniaxial tensile tests were gathered from freshly printed and cross-linked materials. To obtain a better understanding of the dynamic fiber networks, cyclic tensile/compression tests were performed at different strain rates and limits (Figure 3I–K). A strain rate of 200 mm min^{-1} imitates 67 heartbeats per min (BPM). There was a minor nonlinear behavior and plastic deformation observed under these conditions. This nonlinearity is more pronounced at lower strain rates (50 mm min^{-1}) and at higher strains (25 %) for axially printed, axially cut samples Figure 3J. It is proposed that the observed non-linearity is

caused by a change in the network connectivity between ALG and NFC in the first stretching cycle. This cycle seems to break the initial network connectivity upon stretching, followed by a potential curling of the structure upon subsequent compression. The changes in connectivity and network reorientation are obviously also strongly time-dependent and therefore more effective at lower strain rates (Figure 3J,K). For radially aligned axial cut samples, two obvious differences can be seen. Firstly, the maximum tensile stress at 25 % strain is almost half that of the axial fiber orientation. This is consistent with the results from the ultimate tensile strength tests. Secondly, the initial linear elongation curve gives a lower tensile strength than the following cycles (Figure 3K). This behavior can be attributed to an imposed fiber orientation due to stretching, an effect that is known from natural tissue deformed against its predominant fiber orientation.[27]

2.2.3. Pressure Tests

The tested tubes are resistant to water and do not leak up to a few hundred mmHg which is remarkable, given the fact that they are comprised of highly hydrophilic cellulose fibers and alginate. Figure 3B,C show the pressure setup for the expansion tests of the tubes, whereas Figure 3M depicts the ratio between the relative diameter and the height of the tubes in relation to the applied pressure. When a pressure between 60 and 240 mmHg was applied, the tubes with an axial fiber orientation expanded more significantly in radial direction. For radially printed tubes the relative expansion of height and diameter is however similar. The intermediate case is observed for tubes comprising an axial/radial/axial print pattern. For comparison,
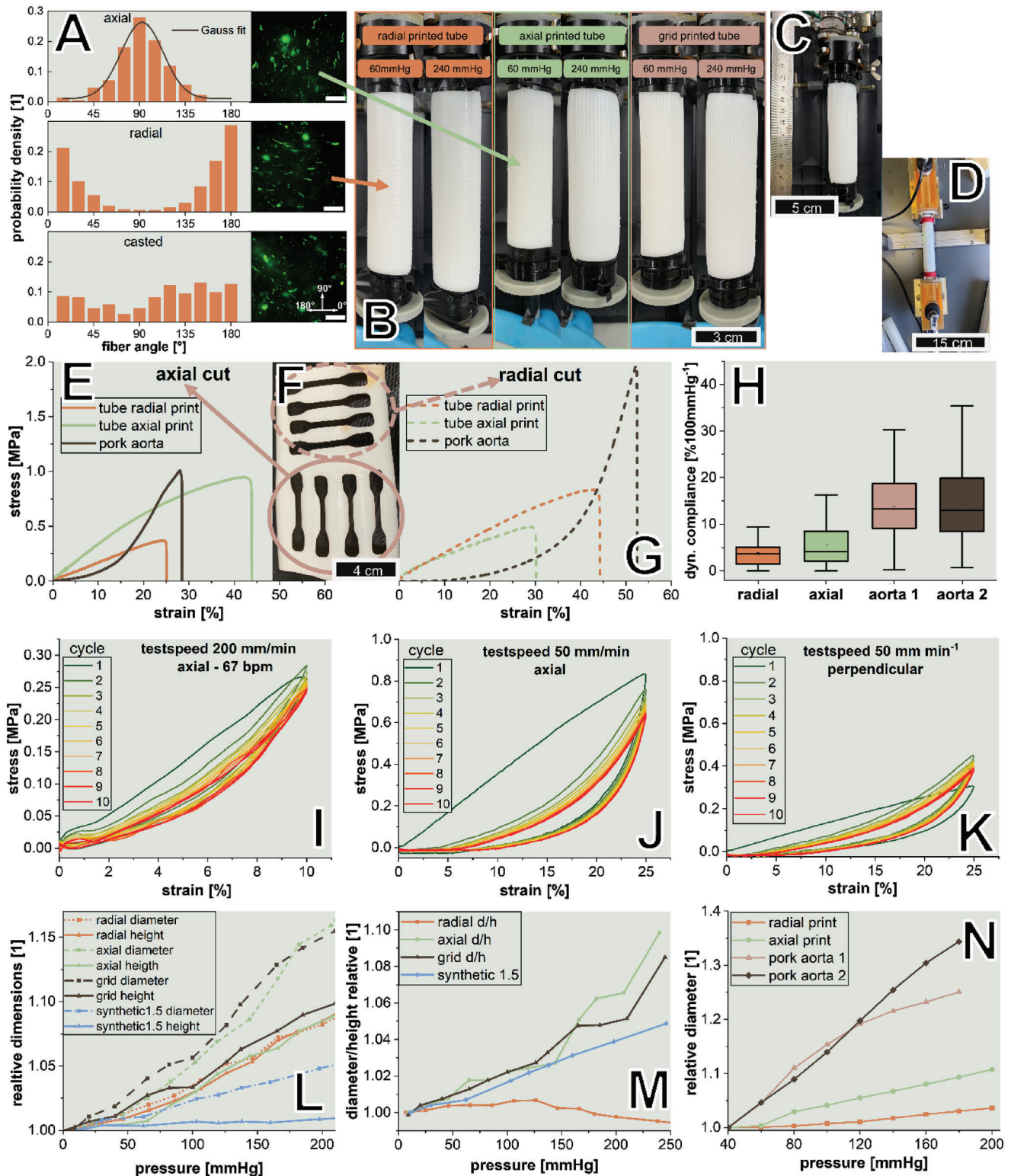
Figure 3. Fiber orientation, pressure expansion measures, and tensile properties of printed tubes and a porcine aorta, A) probability distribution of fiber angles of stained nanocellulose fibers with different printing paths axial (top), radial (center), and cast (bottom), and the corresponding fluorescence microscopy images on the right (scale bar 20 µm), B) images of 3D printed tubes with a radial (left), axial (center), and a grid (right) printing pattern, at two different pressures (60 and 240 mmHg). The radially printed tube expanded predominantly in height, while the axially printed tube expanded more in diameter, and the grid printed one is a mixture of both patterns, C) vertical static pressure test setup allowing elongation and measurement in height and diameter, D) horizontal static and dynamic pressure testing setup allowing continuous measurement under pulsating pressure, E) stress

**ADVANCED
SCIENCE NEWS**

www.advancedsciencenews.com

**ADVANCED
HEALTHCARE
MATERIALS**

www.advhealthmat.de

printed isotropic photopolymer tubes with the same dimensions were tested, which do not show these two extremes of mechanical anisotropy. The axially aligned network is obviously less pressure resistant in the radial direction of the tube, whereas the radially printed tube expands less into the radial direction. This behavior again strongly correlates with the findings of the uniaxial tensile tests, in which the modulus is higher along the fiber direction.

2.2.4. Compliance

Using a measurement setup as shown in (Figure 3D) it was possible to measure the dynamic pulsation of the tubes and porcine aortae. Figure 3N depicts the pressure-dependent changes in the relative diameter of the printed tubes in comparison to the porcine aortae at pressures between 40 and 200 mmHg. The diameter of the axially printed tube increased more steeply, analogous to the experiments with the vertical pressure setup above. However, for the naturally grown blood vessels, the relative diameter increases twice as much as for the printed tubes reflecting the significantly lower modulus of the vessel at lower strains. A similar trend was observed when measuring the dynamic compliance between 120 and 80 mmHg. The radially printed tube proved to be the stiffest with the lowest compliance (3.6 % 100 mmHg^{-1}), followed by the axially printed tube at 5.6 % 100 mmHg^{-1}. The porcine aortae expanded by 13.6 and 14.3 % 100 mmHg^{-1} (Figure 3H) (Videos S3 and S4, Supporting Information). This difference is to some extent due to the relatively high Ca^{2+} content of the Ink1.1, resulting in an approximate Ca^{2+} content of 105 ± 3 µmol g^{-1} for the test setup shown in Figure 3D, in contrast to the Ca^{2+} content in the upright test setup shown in Figure 3C (79 ± 4 µmol g^{-1}). For the influence of Ca^{2+} on the mechanical properties, see Section 2.3.

It is important to note that the porcine aortae are dead tissue, and the data might therefore not reflect the exact compliance, tensile strength, or moduli found in a living animal. The data does not account for smooth muscle tone of the vessel wall and blood flow, or the pressure resistance of the surrounding tissue, which could lead to an overestimation of compliance and extensibility in our experiments. Noninvasive Doppler ultrasound assessments of human aortic compliance give values between 8.4 ± 4.5 and 11.4 ± 4.6 % 100 mmHg^{-1} depending on the patient's cardiovascular risk factors and events.[28] Nevertheless, the printed tubes have similarities to porcine aortae with respect to the ultimate tensile strength, the strain at break, and more importantly the anisotropic strength and moduli distribution.

2.3. Ion Exchange and its Influence on Scaffold Properties

Due to the high water content of about 90 w% after printing and the hydrophilic bio-based materials, the printed hydrogel scaffolds are influenced by the surrounding media.[19] In particular small molecules, (Ca^{2+}, Na^+, water, protons, and anions) can easily diffuse into the hydrogel matrix. Ca^{2+} forms an egg-box structure with sodium alginate and its concentration controls the mechanical properties and density of the gel.[29] The exchange dynamics and stability of Ca^{2+} in the materials are therefore essential.[19] Using two major cations of interest, the approximate ionic strength of blood was imitated (150 mM Na^+ and 2.5 mM Ca^{2+}) with chloride as the anion.[30] Scaffolds printed with Ink1.1 and cross-linked in EtOH/H$_2$O were stored in this solution and in a solution without additional Ca^{2+}. The storage solution was replaced every 24 h and analyzed for calcium leaching. The experiment without calcium in the storage solution leached significant amounts of Ca^{2+} at each cycle, resulting in a cumulative loss of 83.9 ± 1.5 % of the original amount of calcium in the ink after 10 cycles (**Figure 4**A). This leaves a highly swollen scaffold behind which is too unstable to touch or transfer. When calcium is present in the storage solution, the leaching is inhibited, resulting in a leached saturation of 49.3 ± 3.0 % after 10 cycles. Figure 4C shows the amount of the remaining Ca^{2+} in the scaffold in dependence on Ca^{2+} in the storage solution. The initial amount of 110 µmol Ca^{2+} per gram of scaffold could be exceeded after five leaching cycles. This can be explained by the uptake of calcium, but also by the increase in the density of the network represented by an observed mass loss and further shrinkage (Figure 4D). This mass loss is mainly due to the loss of water, and not the loss of polymer, and increases with increasing calcium content in the scaffold. As the networks become denser, the mechanical properties also change. This behavior can be related to the results of the tensile test, where the ultimate tensile strength increases from 0.30 ± 0.05 MPa at low, to 1.63 ± 0.11 MPa at high Ca^{2+} concentrations. At the same time, the experimental tensile modulus increases from 2.87 ± 0.11 to 9.22 ± 0.65 MPa (Figure 4E,F). For most applications, especially in tissue engineering, where the calcium ion concentration cannot be freely chosen, an intermediate concentration of 2.5 mM is suitable for a stable scaffold. However, in the case of continuous rinsing with a NaCl solution, or the absence of Ca^{2+}, disintegration is observed. Samples that are stored in CaCl$_2$ solutions with approximate physiological amounts (0.5 or 1 mM) showed almost no adverse effects on the activated partial thromboplastin time (APTT) with 98 ± 2 % and 97 ± 3 % relative coagulation time compared to the control without scaffold (Figure S3, Supporting

strain curves of cutouts in the axial direction of anisotropic printed tubes cut in axial direction and natural porcine vascular tissue, F) picture of tensile test cutouts of a radially printed tube cut in axial direction, G) stress strain curves of cutouts in the radial direction of anisotropic printed tubes cut in axial direction and natural porcine vascular tissue, strong anisotropic behavior between the different printing methods visible with inversed load bearing directions, H) boxplots of the dynamic compliance measurements between 80 and 120 mmHg of printed tubes and porcine aortae, I) cyclic stress strain curves over 10 repeated cycles with 10 % strain limitation and a test speed of 200 mm min^{-1}, which would correspond to 67 beats per min (BPM), J) cyclic stress stain curves over 10 repeated cycles with 25 % strain limitation, but lower test speed of 50 mm min^{-1}, K) cyclic stress stain curves over 10 repeated cycles with 25 % strain, but with perpendicular fiber orientation compared to the previous tests, resulting in almost half of the tensile modulus, L) graph comparing relative diameter (dotted line) or height (solid line) with applied pressure of tubes printed with Alg-NFC ink (anisotropic) but also with synthetic photopolymer (isotropic), M) graph comparing the ratio of relative diameter divided by relative height and applied pressure to illustrate the strong anisotropic effect caused by the printing process, and N) diagram comparing the diameter of radially and axially printed tubes with pork aortae at different pressures using the horizontal test setup.
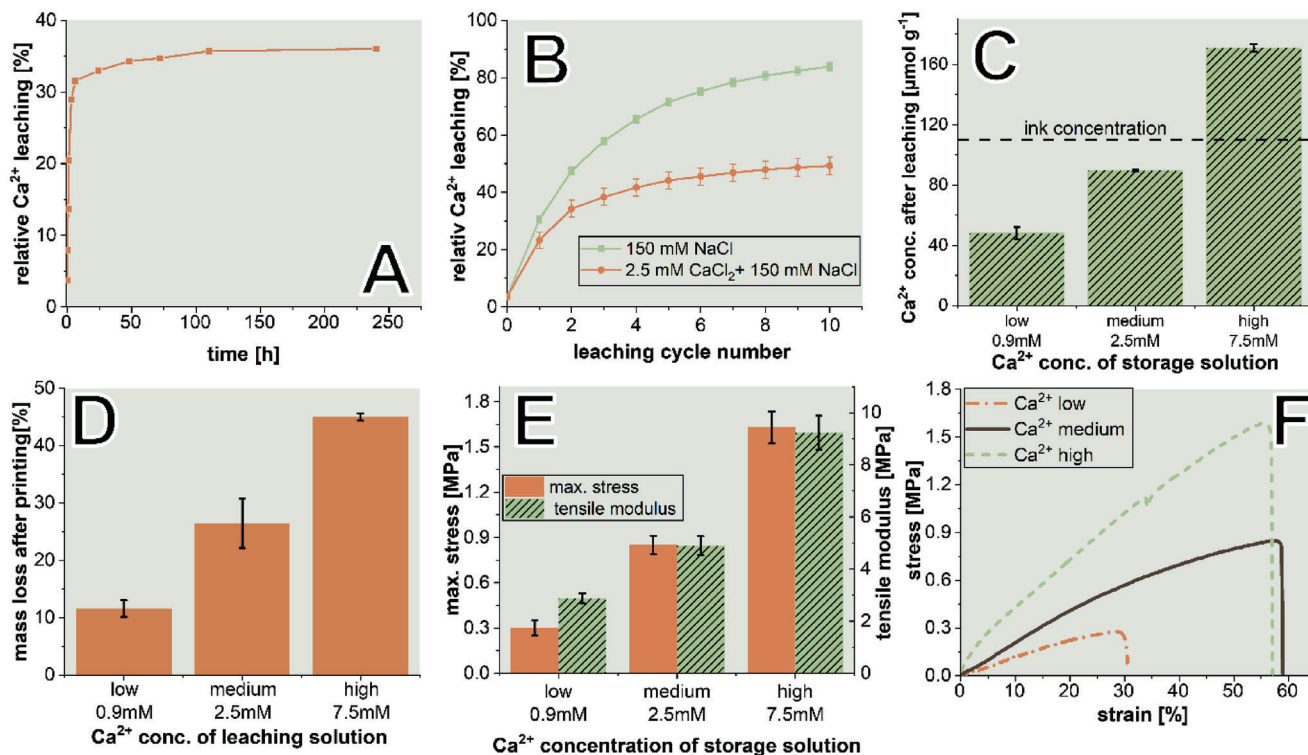
Figure 4. Calcium leaching, and the influence on mechanical performance; A) Simulation of continuous leaching by changing the storage solutions (150 mM NaCl and 150 mM NaCl + 2.5 mM $CaCl_2$) every 24 h and measuring the amount of Ca^{2+} leached into the solution and comparing it with the amount originally present in the cross-linked scaffold to obtain relative values; B) Kinetics of calcium leaching into different storage solutions, by measuring the leached calcium concentration over time; C) Remaining Ca^{2+} concentration in scaffolds leached for five cycles in solutions containing low (0.9 mM), medium (2.5 mM), and high (7.5 mM) Ca^{2+} concentrations, together with 150 mM NaCl in all solutions; D) Mass loss of the scaffolds comparing their weight after printing, and after crosslinking, including leaching of five cycles in the same solutions as in (C); E) Tensile tests of the leached samples from (C); F) Stress-strain curves of the leached samples from (C), showing a strong influence of the stored Ca^{2+} on the toughness and strength of the scaffolds.

Information). However, a high amount of calcium in the scaffold which leaches fast (Figure 4A), results in a very significant increase in the coagulative properties of the material (APTT 28 % of the control). This indicates that the calcium amount used for crosslinking and storage not only strongly influences the scaffold mechanics, but also blood plasma coagulation, and thus could not be freely chosen and must be considered for such applications.

2.4. Controllable Scaffold Degradation

Since the complete removal of calcium ions significantly destabilizes the structure, this property can be used to trigger a controlled disintegration. For certain tissue engineering applications, this controlled degradation is a highly desirable property.[31] In particular, a controlled biocompatible trigger is favorable also because cellulose cannot be hydrolyzed by mammalian cells into glucose. The scaffold can be degraded by reversing the crosslinking process through the removal of Ca^{2+} from the egg box structure. Samples were disintegrated with PBS buffer, sodium citrate, and sodium EDTA, chemicals frequently used in cell cultures (**Figure 5**A). The PBS buffer removes calcium ions from the alginate by forming insoluble, turbid, col-

orless calcium phosphate salts. However, this mechanism acts much slower than complexing the bivalent ion with citrate, or EDTA. In the latter case, only small pieces of the printed tubular scaffolds are left after 6 h, and after 24 h a turbid viscous colorless suspension remains. To completely dissolve the remaining nanocellulose fibers, cellulases from *Trichoderma viride* were added and a clear glucose solution confirmed by NMR and TLC was formed (Figure 5C and Supporting Information). To avoid disintegration in the presence of the above substances, an excess of Ca^{2+} can be added, reaching saturation before Ca^{2+} is displaced from the alginate structure (Figure 5B).

2.5. Nutrient Transport and Diffusion in 3D-Printed Scaffolds

Due to the importance of nutrient diffusion in cell culture,[32] it was estimated how quickly various molecules diffuse through the material clamped between two reservoirs (Figure 5D,E and Supporting Information). Na^+ and Ca^{2+} passed fast enough to reach equilibrium on both sides of the reservoir after 48 h. Riboflavin passed slightly slower than the inorganic ions, but also reached saturation after 48 h, whereas glucose reached 89 % of saturation during the same time. DTAF-labeled 20 kDa dextrans are more hindered and reach a 10 % equilibrium within 48 h whereas BSA
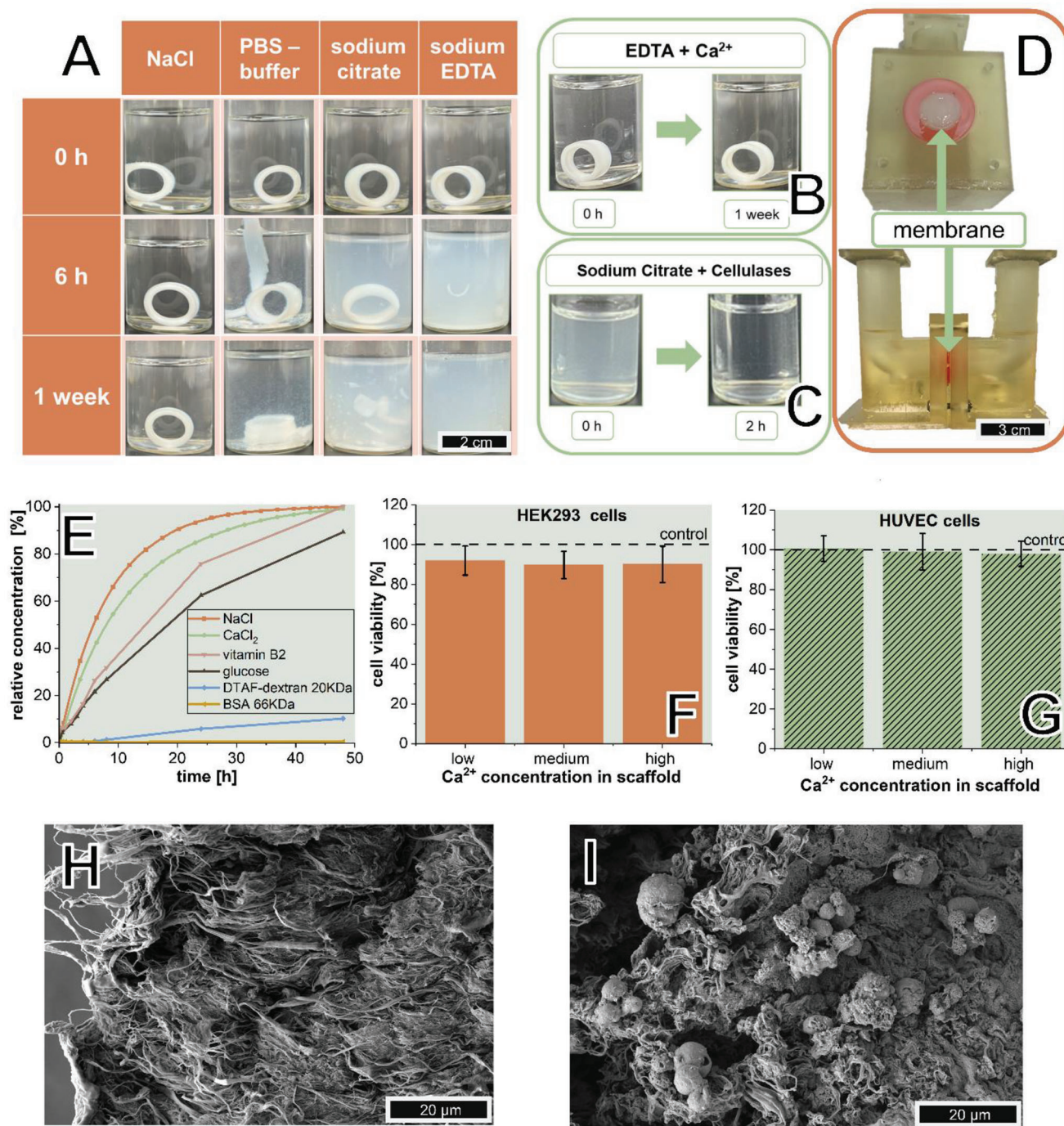
ADVANCED
SCIENCE NEWS
www.advancedsciencenews.com

ADVANCED
HEALTHCARE
MATERIALS
www.advhealthmat.de

Figure 5. Scaffold properties and biocompatibility; A) triggered degradation of the cross-linked scaffold using PBS buffer, citric acid, and EDTA in a four times molar excess and NaCl solution as control without visible change after 1 week, B) inhibition of degradation by an excess of Ca²⁺, C) enzymatic digestion of the dispersed nanocellulose with *Trichoderma viride* cellulases after initial degradation with EDTA to a clear, transparent glucose alginate solution, D) front view of the diffusion cell (top) with the Alg-NFC membrane in the middle and side view (bottom) of the fully assembled cell, E) concentration profiles of various nutrients over time, measured with the diffusion cell, F) cell viability assays using HEK 293 cells and a PrestoBlue assay after 48 h indirect contact with the scaffold containing low (30 µmol g⁻¹), medium (72 µmol g⁻¹), and high (204 µmol g⁻¹) concentration of Ca²⁺ in the scaffold, G) cell viability assays with human umbilical vein endothelial cells (HUVEC) analogous to HEK cells, H) scanning electron micrographs of the native scaffold without cells with fiber orientation in the horizontal direction, and I) scanning electron micrographs with seeded cells.

**ADVANCED
SCIENCE NEWS**

www.advancedsciencenews.com

**ADVANCED
HEALTHCARE
MATERIALS**

www.advhealthmat.de

(66 kDa) did not pass, making the printed membrane a tool for molecular separation.

2.6. Cell Viability of HEK293 Cells and Primary HUVECs

As shown in Section 2.3, the materials can interact with their surroundings by uptake or release of substances. To evaluate if this release can have adverse effects on human cells, three different scaffolds were used with low (30 µmol g^{-1}), medium (72 µmol g^{-1}), and high (204 µmol g^{-1}) concentrations of internal Ca^{2+}. To investigate the harmful effects of the bioink on cell viability, a PrestoBlue assay was performed. Primary human umbilical vein endothelial cells (HUVEC) and immortalized human embryonic kidney cells (HEK293 cell line) were used. From the literature, it is known that NFC and alginate are biocompatible materials that sustain cell viability even after implantation.[23a,26,33] The results from the cytotoxicity analysis show that the co-culture of the different scaffolds has no significant effect on the cell viability compared to the control. After 48 h of incubating the cells with the scaffolds, the cell viability was at least above 90 % (HEK: 92.4 ± 6.7 % [low], 92.8 ± 9.9 % [medium], 90.6 ± 7.4 % [high] and HUVEC: 100.6 ± 6.4 % [low], 99.0 ± 9.1 % [medium], 97.9 ± 6.4 % [high]) (Figure 5F,G). Scaffolds directly seeded with HUVECs were investigated by scanning electron micrographs (SEM) showing cells on the surface in Figure 5I and the bare material as the control in Figure 5H. These findings imply that the prints have the potential to be further investigated in tissue culture applications.

3. Conclusion

With a 4-axis 3D printing method based on a rotating drum and a bioink extrusion head, nanofibrillar cellulose/alginate gels can be aligned into stable, cross-linked tubular forms that resist water pressures up to 500 mmHg. Nanofibrillar anisotropy and ionic crosslinking can be used to adjust the macroscopic expansability and compliance of the tubes and to manufacture tissue mimetic biomaterials. Various tubular shapes with a similar elongation, ultimate tensile strength, and compliance as a porcine aorta can be manufactured reproducibly. Since the cross-linking is based on the ionic complexation of alginate, the bonds can be reversibly broken using small molecular complexing agents, whereas the remaining cellulose fibers can be decomposed into glucose with the aid of cellulases. High calcium ion concentrations are however impacting blood plasma coagulation, and more research on the interactions of the materials with cells, tissue, and whole organisms is necessary. The non-toxic materials are permeable by small molecules relevant for tissue culture and have a molecular weight cut-off of ≈20 kDa. The method of manufacturing combined with the properties of the nanomaterials appears to have a high potential to be applied as vascular tube models in presurgical planning or as tissue culture substrates. The latter has been shown for non-anisotropic NFC and alginate combinations in several studies, whereas the former has, to our knowledge, not been reported anywhere. It is proposed here that after careful validation, of our plant-based tissue imitates could substitute cruel animal studies in some cases. Investigations into these applications are part of the ongoing work at our laboratories.

Table 1. Preparation of nanocomposite inks for DIW 3D printing.

Inks	NFC		Alg		CaCO$_3$ NPs	
	[g]	[w%]	[g]	[w%]	[g]	[w%]
Ink0.3	20	2.8	1.33	6.2	0.060	0.3
Ink1.1	20	2.8	1.33	6.2	0.220	1.1
Ink3.3	20	2.8	1.33	6.2	0.660	3.3

4. Experimental Section

Materials: NFC suspension (3 w% solid content) was purchased from the University of Maine, USA (R-COO⁻ 0.35 ± 0.05 mmol g^{-1}). Sodium alginate from brown algae (COONa: 2.63 ± 0.12 mmol g^{-1}), glucono-δ-lactone (Gdl, ≥ 99 %), ethylenediaminetetraacetic acid disodium salt dihydrate (Na$_2$EDTA*2H$_2$O, ≥ 99 %), calciumchloride (CaCl$_2$, 99 %), 5-([4,6-dichlorotriazin-2-yl]amino)fluorescein hydrochloride (DTAF, ≥ 90 %), cellulases from *T. viride* (3-10 U g^{-1}), and calconcarboxylic acid were purchased from Sigma-Aldrich, Austria. Calcium carbonate nanoparticles (CaCO$_3$ NPs, 99.5 %) were purchased from Solvay Chemicals International, Belgium. Ethanol (≥ 99 %) was purchased from VWR Chemicals. Gibco DMEM/F12 media, Gibco fetal bovine serum (FBS), P/S 100× solution, and Pierce BCA Protein Assay Kit were purchased from Thermo Fisher Scientific. Hydrochloric acid (HCl, 37 w%), and sodium hydroxide (NaOH, ≥ 98 %) were purchased from Fisher Scientific. Glucose (> 99 %), bovine serum albumin NZ-origin 66 kDa, dextran 20 kDa, riboflavin (> 97 %), sodium chloride (≥ 99 %), and citric acid monohydrate (≥ 99.5 %) were purchased from Carl Roth. PrestoBlue cell viability reagent was purchased from Invitrogen. HUVECs and HEK293 cells were purchased from Promocell, Heidelberg and Biobank Graz. SmoothFlow tapered tips (250 and 410 µm), syringe barrel pistons, and fluid dispensing polyethylene-based plastic cartridges were purchased from Nordson, UK. ECO Resin (black, gray, and transparent) was purchased from Anycubic, China. EcoPLA (food grade) – filament was purchased from 3DJake, Austria.

Preparation of Inks for Direct-Ink-Writing (DIW): The general procedure was described in a previous paper.[19] Briefly, 20.0 g nano-fibrillated cellulose (NFC) with a solid content of 3.0 w% in water was mixed with the appropriate amounts of CaCO$_3$ (**Table 1**) at 2000 rpm for 60 s in a 50 mL Falcon tube using a 3D-printed stirrer. To the homogeneous ink, 1.33 g of Na-alginate (Alg) was added and mixed for 10 min to be used directly for printing.

DIW 3D Printing: 3D models were generated using the open-source program FreeCAD 0.19 or 3D Builder 18.0.1931.0 (Microsoft Corporation). Regardless of the printing technique, the composite inks were extruded from a 30 mL polyethylene-based plastic barrel (Nordson, U.K Limited) equipped with tapered tips (Nordson, UK Limited) with an inner diameter of 410 µm using a GeSiM Robotics BioScaffolder 3.2 (GeSIM, Germany) including its own software.

Printing of Flat Structures: Simple sheets with 58 × 16 × 2.0 mm³ for tensile tests or discs with 28 × 2.0 mm² (diameter × height) for cell tests were printed on polystyrene Petri dishes. Extrusion pressures between 130–160 kPa, strand distances of 0.5 mm, strand height, and width of 0.44 mm, with a printing speed of 25 mm s^{-1}. Depending on the desired fiber orientation different printing patterns were used by either rotating each subsequent layer 90° or keeping it constant.

Printing of Tubes: A rotating auxiliary axis was built (Figure 2A). Briefly, it consisted of a 3D printed core unit holding three 8 mm ball bearings and a Nema 17 stepper motor (Stepperonline, China) which drove a 8 mm stainless steel shaft. 3D-printed cylinders of various diameters could be attached to the end of this shaft. The rotation movement of this auxiliary axis was controlled by an Arduino UNO board (Arduino, Italy) together with an L293D Motor Driver Shield (AZDelivery, Germany) and a self-built photoelectric switch. For the radial print pattern, the linear speed of the printing head was coordinated with the rotation speed of the drum to reach 20 mm s^{-1} radial printing speed. For the linear print pattern, double

strands with 20 mm s^{-1} printing speed were printed at each incremental movement. All other settings were used according to the printing of flat structures.

Ionic Crosslinking: All freshly printed scaffolds were subsequently crosslinked by fully submerging them into a solution of ethanol/water (50/50 w%) together with 4.00 mol. equiv. of GdL with respect to CaCO$_3$ for 24 h under gentle shaking with a Unimax 2010 (Heidolf, Germany) at ambient conditions. The mass ratio of scaffold to crosslinking solution was 1 to 10.

Post Treatment and Leaching: All samples could be stored after crosslinking in a solution of ethanol/water (50/50 w%) without losing their mechanical stability.[19] To simulate physiological osmotic conditions, the samples were stored in a 150 mM NaCl solution with the addition of different concentrations of CaCl$_2$ to control the leached amount of Ca^{2+} ions and subsequently the remaining calcium in the scaffold. A tenfold excess of leaching solution with respect to the wet scaffold mass was used. The leached amount of calcium in the solution as well as in the scaffold analyzed by volumetric titration using Na$_2$EDTA and an already established protocol from a previous work.[19]

Mechanical Testing: Dog bone-shaped tensile test specimens were punched out from 3D printed scaffolds and porcine aortae (50 × 8.5 × 1.00–2.50 mm^3) according to DIN 53504 S3A. A Shimanzu AGS-X (Japan) tensile testing machine equipped with a 5 KN load cell was used to perform tensile and cycle tests at speeds between 10 and 200 mm s^{-1}. All experiments were performed in quadruplicates.

Static Pressure Tube Testing: Tubes with axial, radial, and grid printing paths were produced using Ink1.1 and a 22 mm diameter rotating drum. While all three layers were aligned equally for axially and radially aligned tubes, the alignment was alternated for grid-printed tubes (linear-radial-linear). After 24 h of crosslinking, the tubes were stored in a 2.5 mM CaCl$_2$ solution along with 150 mM NaCl. After 24 h, this leaching solution was changed five times. This resulted in tubes with an inner diameter of 22 mm and a wall thickness of 1.5 ± 0.1 mm. The tubes were mounted on a 3D-printed connector that allowed pressure measurement with an M3200 pressure sensor controlled by an Arduino UNO (Arduino, Italy). While the lower end of the tube was sealed with a 3D-printed plug, a tube containing storage fluid was mounted to the upper port, which was connected to a controllable nitrogen gas supply. The filled tube was pressurized in increments of 20 mmHg and an image was acquired after 60 s of stabilization. After a recovery time of 60 s at 0 mmHg, each cycle was repeated. The height and diameter of the tube could be determined without contact from the images using Image J 1.53 (National Institute of Health, USA).

Dynamic Tube Measurement and Compliance: For the dynamic compliance measurements, tubes were inserted in a vascular flow setup comprised of two A-10 pressure sensors (Wika, Germany), a laser micrometer LS7070MR (Keyence, Japan), a ventricular assisting device Excor VAD 60 mL (Berlin Heart, Germany) as a pulsating pump, and variable resistance connected to a reservoir. The ventricle of the pump was agitated at a rate of 60 bpm, to create a systolic pressure of 120 mmHg in the tubes and dropping to a diastolic pressure of 80 mmHg during ventricle retraction. For each specimen, the dynamic compliance was measured for 5 min. Together with the NFC-Alg tubes, porcine aortae (16 cm length, aortic diameter ≈2 cm, aortic wall thickness ≈2 mm) freshly received from the local slaughterhouse were measured. For these experiments, no ethical approval was necessary. With the same setup, static compliance was measured creating a constant pressure in the range of 20–200 mmHg with increments of 20 mmHg. However, with this method, only a diameter-to-pressure measurement could be performed lacking the height measurement in comparison with the static pressure testing. The compliance is calculated according to Equation S3, Supporting Information)

Cell Viability, Plasma Coagulation and SEM: Prior to cell testing 3D printed discs with 28 × 0.8 mm (diameter × height) were stored in 0.5 mM (low), 1.0 mM (medium), and 5.5 mM (high) CaCl$_2$ solution including 150 mM NaCl. Complete storage solution change was repeated five times after 24 h each to control the calcium concentration of the scaffolds. After the last leaching step, small discs with a diameter of 6 mm were punched out and autoclaved at 125 °C for 15 min. The remaining amount of calcium in the samples was analyzed by titration with 30, 72, and 204 µmol g^{-1}

for low, medium, and high calcium concentrations. To estimate the blood plasma coagulative properties of the materials, the cut samples with 15–19 mg wet mass were brought in direct contact with a tenfold amount of blood plasma (Coag-Control P, Stago) for 10 min at 37 °C. Afterward, a standardized activated partial thromboplastin time test (APTT) using a Stago Start Max and the C.K. Prest method was performed. In short, 50 µL of the plasma and 50 µL of C.K. Prest solution were incubated 180 s and the coagulation time was measured after the addition of 50 µL STA CaCl$_2$ 0.025 M solution. For each calcium concentration, three samples were measured in triplicates and compared to the control sample without a scaffold.

To test whether the discs release any substance that may have a cytotoxic effect on cells, a transwell cytotoxicity test was performed. Briefly, HEK293 cells were cultured in Dulbecco's modified Eagle medium/nutrient mixture F-12 (DMEM/F12) supplemented with 1 % penicillin/streptomycin solution and 10% fetal bovine serum. Primary HUVECS (Promocell, Heidelberg, Germany) were cultured in endothelial cell growth media supplemented with 1 % P/S. A monolayer culture of each cell type was seeded onto the bottom of a 24-well plate (4 × 10^4 cells per well) and grown until reaching a confluency of at least 60–70 %. Each chamber of the plate had an insert with a semi-permeable membrane to separate the cells from direct contact with the disc. After an incubation of 48 h, the cell survival percentage was quantified by using the PrestoBlue cell viability reagent (MolecularProbes by Life Technologies, CA, USA). This reagent was a cell-permeable resazurin-based solution that was rapidly reduced by metabolically active cells and the absorbance was measured at 570/600 nm (excitation/emission) with a SpectraMax iD3 plate reader (MolecularDevices, CA, USA). Three independent experiments were performed, and each experiment included three technical replicates as well. Cells without the addition of a scaffold were used as negative control and indicated as 100 % viable.

For scanning electron microscopy HUVEC 3D printed scaffolds were fixed in 2 % paraformaldehyde/2.5 % glutaraldehyde for 2 h, post-fixed with 2 % osmium tetroxide for 2 h at room temperature, and subsequently dehydrated in graded ethanol series (30-96 % and 100 % (vol/vol) EtOH). HMDS (VWR International, LLC.) drying and sputter coating (Bal-Tec Sputter Coater 500) were applied afterward. Further, scaffolds were placed on stubs covered with conductive double-coated carbon tape. The images were taken with a Sigma 500VP FE-SEM with an SEM detector (Zeis, Oberkochen) operated at an acceleration voltage of 5 kV.

Optical Fiber Orientation Analysis: A standard ink containing 0.03 w% self-synthesized DTAF-NFC (**SI**) was prepared as described above. Tensile test sheets were printed using 135 kPa extrusion pressure with a 410 µm nozzle and 20 mm s^{-1} printing speed. After 24 h, crosslinking microscopic images were taken using a Panthera Tec-Mat-BT (Motic, China) equipped with an EPI fluorescence module for FITC. A minimum of 500 fibers were analyzed by measuring the fiber angle with Image J 1.53 (National Institute of Health, USA).

Nutrient Diffusion: A diffusion cell consisting of two symmetrical parts was designed using FreeCad 0.19 and printed using an LCD 3D printer (Anycubic, China). The two cells were sealed with silicone gaskets and the NFC-Alg membrane was put in the middle and pressed together with four M3 screws to seal them completely. The printed membrane was a flat round disc 28 mm in diameter with two layers of height with a grid printing pathway and without gaps between the strands, resulting in a membrane thickness of 0.80–1.20 mm^2 after ion crosslinking. Standard Ink1.1 was used with the crosslinking method described above. Both sides of the cells were filled with 10 mL MilliQ water or buffer corresponding to the analyte. Concentrated analyte was added to one side of the cell and the concentration was monitored over time. Magnetic stir bars 10 mm long were placed on both sides of the cell and driven to 200 rpm by a magnetic stirrer located below to avoid bulk diffusion limitations. For NaCl and CaCl$_2$, conductivity was measured at 10 s intervals, whereas for bovine serum albumin, DTAF-dextran, glucose, and riboflavin, samples were taken manually from both sides at 0.5, 1, 2, 4, 6, 8, 24, and 48 h. Concentrations of analytes were measured by a BCA assay for BSA, fluorescence spectroscopy for DTAF-dextran and riboflavin, and refractometry for glucose. Detailed description in the Supporting Information.

**ADVANCED
SCIENCE NEWS**

www.advancedsciencenews.com

**ADVANCED
HEALTHCARE
MATERIALS**

www.advhealthmat.de

Controlled Degradation and Stability: Short tubes (ID 9 mm, OD 12 mm, height 5–6 mm) were printed using Ink1.1 and crosslinked as described above. The tubes with 300 ± 50 mg mass were placed in 20 mL caped glasses with 10 mL of 150 mM NaCl and 4 mol. equivalents of a) PBS-buffer salts, b) citric acid, c) Na_2EDTA, and d) nothing as control, with respect to the $CaCO_3$ amount were added. (Table S2, Supporting Information) The pH value of all solutions was adjusted to 7.0 using NaOH and the solutions were gently shaken at room temperature. For the subsequent digestion of the remaining NFC, scaffolds previously fully disintegrated with EDTA were brought to pH 5.2, and 10 mg (30–100 units) cellulase isolated from *T. viride* was added. After 12 h, a completely clear solution was observed. The conversion to glucose was confirmed via TLC and NMR spectroscopy (Supporting Information).

Supporting Information

Supporting Information is available from the Wiley Online Library or from the author.

Conflict of Interest

The authors declare no conflict of interest.

Data Availability Statement

The data that support the findings of this study are available from the corresponding author upon reasonable request.

Keywords

[1] A. Tsamis, J. T. Krawiec, D. A. Vorp, *J. R. Soc., Interface* **2013**, *10*, 20121004.

[2] a) Y. Liu, S.-H. Lin, W.-T. Chuang, N.-T. Dai, S.-H. Hsu, *ACS Appl. Mater. Interfaces* **2022**, *14*, 16032; b) G. Singh, A. Chanda, *Biomed. Mater.* **2021**, *16*, 062004; c) S. S. Sheiko, A. V. Dobrynin, *Macromolecules* **2019**, *52*, 7531; d) C. F. Guimarães, L. Gasperini, A. P. Marques, R. L. Reis, *Nat. Rev. Mater.* **2020**, *5*, 351.

[3] a) S. Sherifova, G. A. Holzapfel, *Prog. Biomed. Eng.* **2020**, *2*, 032002; b) D. B. Camasão, D. Mantovani, *Mater. Today Bio* **2021**, *10*, 100106.

[4] a) C. Storm, J. J. Pastore, F. C. MacKintosh, T. C. Lubensky, P. A. Janmey, *Nature* **2005**, *435*, 191; b) F. Burla, S. Dussi, C. Martinez-Torres, J. Tauber, J. van der Gucht, G. H. Koenderink, *Proc. Natl. Acad. Sci. U. S. A.* **2020**, *117*, 8326; c) R. E. Shadwick, *Shiyan Shengwu Xuebao* **1999**, *202*, 3305.

[5] Y. Li, Y. Xiao, C. Liu, *Chem. Rev.* **2017**, *117*, 4376.

[6] a) S. Abdollahi, J. Boktor, N. Hibino, *Transl. Res.* **2019**, *211*, 123; b) H. Su, Q. Li, D. Li, H. Li, Q. Feng, X. Cao, H. Dong, *Mater. Horiz.* **2022**, *9*, 2393.

[7] a) L. Severseike, V. Lee, T. Brandon, C. Bakken, V. Bhatia, *bioRxiv* **2019**, 825794; b) M. Grab, C. Hopfner, A. Gesenhues, F. König, N. A. Haas, C. Hagl, A. Curta, N. Thierfelder, *J. Vis. Exp.* **2021**, *167*, 62063.

[8] M. Vatankhah-Varnosfaderani, W. F. M. Daniel, M. H. Everhart, A. A. Pandya, H. Liang, K. Matyjaszewski, A. V. Dobrynin, S. S. Sheiko, *Nature* **2017**, *549*, 497.

[9] K. Wang, C.-C. Ho, C. Zhang, B. Wang, *Engineering* **2017**, *3*, 653.

[10] a) M. Vatankhah-Varnosfaderani, A. N. Keith, Y. Cong, H. Liang, M. Rosenthal, M. Sztucki, C. Clair, S. Magonov, D. A. Ivanov, A. V. Dobrynin, S. S. Sheiko, *Science* **2018**, *359*, 1509; b) D. Zhalmuratova, H.-J. Chung, *ACS Appl. Polym. Mater.* **2020**, *2*, 1073.

[11] K. A. Erk, K. J. Henderson, K. R. Shull, *Biomacromolecules* **2010**, *11*, 1358.

[12] a) X. Yang, S. K. Biswas, J. Han, S. Tanpichai, M.-C. Li, C. Chen, S. Zhu, A. K. Das, H. Yano, *Adv. Mater.* **2021**, *33*, 2002264; b) F. Rol, M. N. Belgacem, A. Gandini, J. Bras, *Prog. Polym. Sci.* **2019**, *88*, 241; c) L. Geurds, J. Lauko, A. E. Rowan, N. Amiralian, *J. Mater. Chem. A* **2021**, *9*, 17173.

[13] M. Gao, J. Li, Z. Bao, M. Hu, R. Nian, D. Feng, D. An, X. Li, M. Xian, H. Zhang, *Nat. Commun.* **2019**, *10*, 437.

[14] a) K. J. De France, T. Hoare, E. D. Cranston, *Chem. Mater.* **2017**, *29*, 4609; b) T. Li, C. Chen, A. H. Brozena, J. Y. Zhu, L. Xu, C. Driemeier, J. Dai, O. J. Rojas, A. Isogai, L. Wågberg, L. Hu, *Nature* **2021**, *590*, 47.

[15] G. K. Tummala, T. Joffre, R. Rojas, C. Persson, A. Mihranyan, *Soft Matter* **2017**, *13*, 3936.

[16] J. Wu, Y. Zheng, Z. Yang, Q. Lin, K. Qiao, X. Chen, Y. Peng, *RSC Adv.* **2014**, *4*, 3998.

[17] X. Yang, H. Yano, K. Abe, *Cellulose* **2021**, *28*, 1489.

[18] a) F. Zhou, S. Wu, C. Rader, J. Ma, S. Chen, X. Yuan, E. J. Foster, *Fibers Polym.* **2020**, *21*, 45; b) T. Benselfelt, J. Engström, L. Wågberg, *Green Chem.* **2018**, *20*, 2558; c) N. E. Zander, H. Dong, J. Steele, J. T. Grant, *ACS Appl. Mater. Interfaces* **2014**, *6*, 18502; d) X. Deng, B. Huang, Q. Wang, W. Wu, P. Coates, F. Sefat, C. Lu, W. Zhang, X. Zhang, *ACS Sustainable Chem. Eng.* **2021**, *9*, 3070; e) Y. Yue, J. Han, G. Han, A. D. French, Y. Qi, Q. Wu, *Carbohydr. Polym.* **2016**, *147*, 155; f) M. Bordoni, E. Karabulut, V. Kuzmenko, O. Pansarasa, C. Cereda, P. Gatenholm, *Cells* **2020**, *9*, 682.

[19] F. Lackner, I. Knechtl, M. Novak, C. Nagaraj, A. Dobaj Štiglic, R. Kargl, A. Olschewski, K. Stana Kleinschek, T. Mohan, *Adv. Mater. Technol.* **2023**, *8*, 2201708.

[20] a) F. L. Ronzoni, F. Aliberti, F. Scocozza, L. Benedetti, F. Auricchio, M. Sampaolesi, G. Cusella, I. N. Redwan, G. Ceccarelli, M. Conti, *J. Tissue Eng. Regener. Med.* **2022**, *16*, 484; b) P. Apelgren, M. Amoroso, A. Lindahl, C. Brantsing, N. Rotter, P. Gatenholm, L. Kölby, *PLoS One* **2017**, *12*, 0189428; c) D. Stanco, M. Boffito, A. Bogni, L. Puricelli, J. Barrero, G. Soldati, G. Ciardelli, *Int. J. Mol. Sci.* **2020**, *21*, 8694; d) A. C. Fonseca, F. P. W. Melchels, M. J. S. Ferreira, S. R. Moxon, G. Potjewyd, T. R. Dargaville, S. J. Kimber, M. Domingos, *Chem. Rev.* **2020**, *120*, 11093.

[21] a) O. Fourmann, M. K. Hausmann, A. Neels, M. Schubert, G. Nyström, T. Zimmermann, G. Siqueira, *Carbohydr. Polym.* **2021**, *259*, 117716; b) A. S. Gladman, E. A. Matsumoto, R. G. Nuzzo, L. Mahadevan, J. A. Lewis, *Nat. Mater.* **2016**, *15*, 413; c) G. Siqueira, D. Kokkinis, R. Libanori, M. K. Hausmann, A. S. Gladman, A. Neels, P. Tingaut, T. Zimmermann, J. A. Lewis, A. R. Studart, *Adv. Funct. Mater.* **2017**, *27*, 1604619; d) A. Schwab, C. Hélary, R. G. Richards, M. Alini, D. Eglin, M. D'Este, *Mater. Today Bio* **2020**, *7*, 100058; e) P. Siqueira, É. Siqueira, A. E. De Lima, G. Siqueira, A. D. Pinzón-Garcia, A. P. Lopes, M. E. C. Segura, A. Isaac, F. V. Pereira, V. R. Botaro, *Nanomaterials* **2019**, *9*, 78; f) M. K. Hausmann, P. A. Rühs, G. Siqueira, J. Läuger, R. Libanori, T. Zimmermann, A. R. Studart, *ACS Nano* **2018**, *12*, 6926.

[22] a) T. H. Jovic, T. Nicholson, H. Arora, K. Nelson, S. H. Doak, I. S. Whitaker, *Carbohydr. Polym.* **2023**, *321*, 121261; b) H. Martínez Ávila, S. Schwarz, N. Rotter, P. Gatenholm, *Int. J. Bioprint.* **2016**, *1-2*, 22; c) D. Nguyen, D. A. Hägg, A. Forsman, J. Ekholm, P. Nimkingratana, C. Brantsing, T. Kalogeropoulos, S. Zaunz, S. Concaro, M. Brittberg, A. Lindahl, P. Gatenholm, A. Enejder, S. Simonsson, *Sci. Rep.* **2017**, *7*, 658.

[23] a) P. Apelgren, M. Amoroso, K. Säljö, A. Lindahl, C. Brantsing, L. Stridh Orrhult, K. Markstedt, P. Gatenholm, L. Kölby, *J. Biomed.*

2302348 (11 of 12)

Mater. Res., Part B **2021**, *109*, 126; b) R. Yang, R. Wang, S. Abbaspoor, M. Rajan, A. Turki Jalil, M. Mahmood Saleh, W. Wang, *Arabian J. Chem.* **2023**, *16*, 104799; c) Z. Zhou, A. Zhou, A. T. Jalil, M. M. Saleh, C. Huang, *Bioprocess Biosyst. Eng.* **2023**, *46*, 577.

[24] a) G. Janarthanan, S. Lee, I. Noh, *Adv. Funct. Mater.* **2021**, *31*, 2104441; b) L. Li, S. Qin, J. Peng, A. Chen, Y. Nie, T. Liu, K. Song, *Int. J. Biol. Macromol.* **2020**, *145*, 262; c) H. Liu, H. Zhou, H. Lan, T. Liu, X. Liu, H. Yu, *Micromachines* **2017**, *8*, 237.

[25] T. C. Gasser, R. W. Ogden, G. A. Holzapfel, *J. R. Soc., Interface* **2006**, *3*, 15.

[26] P. Siqueira, É. Siqueira, A. E. E. Lima, G. Siqueira, A. D. Pinzón-Garcia, A. P. Lopes, M. E. C. Segura, A. Isaac, F. V. Pereira, V. R. Botaro, *Nanomaterials* **2019**, *9*, 78.

[27] a) F. Burla, Y. Mulla, B. E. Vos, A. Aufderhorst-Roberts, G. H. Koenderink, *Nat. Rev. Phys.* **2019**, *1*, 249; b) M. E. Susilo, J. A. Paten, E. A. Sander, T. D. Nguyen, J. W. Ruberti, *Interface Focus* **2016**, *6*, 20150088.

[28] E. D. Lehmann, K. D. Hopkins, A. Rawesh, R. C. Joseph, K. Kongola, S. W. Coppack, R. G. Gosling, *Hypertension* **1998**, *32*, 565.

[29] O. Aarstad, E. B. Heggset, I. S. Pedersen, S. H. Bjørnøy, K. Syverud, B. L. Strand, *Polymers* **2017**, *9*, 378.

[30] N. Nezafati, F. Moztarzadeh, S. Hesaraki, *Biotechnol. Bioprocess Eng.* **2012**, *17*, 746.

[31] S. Tajvar, A. Hadjizadeh, S. S. Samandari, *Int. Biodeterior. Biodegrad.* **2023**, *180*, 105599.

[32] a) T. S. Karande, J. L. Ong, C. M. Agrawal, *Ann. Biomed. Eng.* **2004**, *32*, 1728; b) D. S. Masson-Meyers, L. Tayebi, *J. Tissue Eng. Regener. Med.* **2021**, *15*, 747.

[33] a) J. S. Kjesbu, D. Zaytseva-Zotova, S. Sämfors, P. Gatenholm, C. Troedsson, E. M. Thompson, B. L. Strand, *Carbohydr. Polym.* **2022**, *286*, 119284; b) M. Park, D. Lee, J. Hyun, *Carbohydr. Polym.* **2015**, *116*, 223; c) P. Laurén, P. Somersalo, I. Pitkänen, Y.-R. Lou, A. Urtti, J. Partanen, J. Seppälä, M. Madetoja, T. Laaksonen, A. Mäkitie, M. Yliperttula, *PLoS One* **2017**, *12*, 0183487.